3D X-ray Microtomography Volume Correlation to Study Fatigue Crack Growth

N. Limodin, Julien Réthoré, Jean-Yves Buffiere, François Hild, Wolfgang Ludwig, Johann Rannou, Stéphane Roux

3D X-ray Microtomography Volume Correlation to Study Fatigue Crack Growth

By *Nathalie Limodin, Julien Réthoré, Jean-Yves Buffière, François Hild, Wolfgang Ludwig, Johann Rannou* and *Stéphane Roux*

Global digital volume correlation is used to analyze a series of computed tomography images of a nodular graphite cast iron specimen subjected in situ to a fatigue test. From the obtained displacement field, a specific procedure is implemented to extract stress intensity factors all along the crack front. The proposed methodology allows one to measure key parameters in fatigue crack propagation directly from 3D images.

The dramatic human and environmental risks resulting from possible failures due, for instance, to cracks in aeronautic or nuclear structures, justify the amount of work dedicated to the improvement of their safety. The ability of predicting the lifetime of a component requires both material and mechanical knowledge in experimental, theoretical, and numerical fields. Many factors influence the crack growth rate under cyclic loading and lead to retardation or acceleration effects linked to crack closure and small scale yielding, combined loading and bifurcation.[1] Recent experimental facilities such as X-ray synchrotrons or lab tomographs allow for *in situ* and continuous monitoring of crack growth in opaque materials, and offer new possibilities in the understanding of fracture mechanisms.

X-ray computed microtomography is becoming useful for studying many materials.[2,3] In particular, it has been used to analyze cracks in opaque materials. For instance, microcracking in various composites[4–9] or cementitious materials[10] could be visualized. From these observations, a coupling with numerical simulations was shown to be possible.[11] Crack openings were also determined by direct analysis of reconstructed volumes,[12,13] and stress intensity factors (SIFs) were estimated at the tip of a crack in an aluminum sample under increasing load by tracking manually the displacement of small porosities.[14] In the present paper, it is proposed to resort to correlation techniques applied to reconstructed volumes[15] at different loading stages for the analysis of fatigue crack growth. This information gives access to crack opening displacements (CODs) and SIFs, thereby enabling for a *quantitative* analysis of crack propagation.

In order to characterize fatigue cracks, it is proposed to estimate quantitatively displacement fields around cracks using digital volume correlation (DVC). The displacement field is computed so that the image of the loaded sample is matched to the reference image when voxel locations are corrected for by the estimated motion. The most commonly used digital image correlation (DIC) algorithms consist in matching locally small zones in a sequence of pictures to determine local displacement components.[16] The same type of hypotheses is made in three-dimensional DVC algorithms.[17–19] In the present study, a different algorithm is used, namely a Galerkin approach to DIC that was shown to be more performing in two dimensions when compared to traditional DIC algorithms.[20] It has been recently extended to 3D displacements.[15]

Dr. S. Roux, Dr. F. Hild
Laboratoire de Mécanique et Technologie (LMT-Cachan), ENS de Cachan/ CNRS-UMR 8535/Université Paris 6/PRES UniverSud Paris, 61 avenue du Président Wilson F-94235 Cachan Cedex, (France)
E-mail: stephane.roux@lmt.ens-cachan.fr
Dr. N. Limodin, Prof. J.-Y. Buffière, Dr. W. Ludwig
Laboratoire Matériaux, Ingénierie et Sciences (MATEIS), INSA-Lyon/UMR CNRS 5510 7, avenue Jean Capelle, F-69621 Villeurbanne, (France)
Dr. J. Réthoré, Dr. J. Rannou
Laboratoire de Mécanique des Contacts et des Structures (LaMCoS) INSA-Lyon/UMR CNRS 5259, 20 avenue Albert Einstein, F-69621 Villeurbanne, (France)
Dr. W. Ludwig
European Synchrotron Radiation Facility/Experimental Division (ESRF), BP 220 6 rue J. Horowitz, F-38043 Grenoble Cedex, (France)

This work was funded by the CETIM Foundation grant entitled PROPAVANFIS: 'Advanced methods for the experimental and numerical analyses of crack propagations under complex loadings.' This work was also made possible by an ESRF grant for the experiment MA-501 on ID19 beamline.

The paper is organized as follows. First, the experimental procedure is discussed. From computed tomographic images, and by using DVC, 3D displacement fields are obtained and subsequently analyzed. In particular, CODs are determined to study crack characteristics under load at different stages of crack propagation. SIFs are also evaluated thanks to a post-processing of the displacement measurements. Crack propagation features are discussed by using all the previous results.

Materials and Methods

Material and Specimen Preparation

The studied material is a nodular graphite cast iron (3.65 wt% C, 3.2 wt% Si, 0.04 wt% Mg, <0.1 wt% Mn, <0.005 wt% S, 0.02 wt% P) for which the random dispersion of graphite nodules provides a fine 3D random texture that is very well suited for image correlation. Casting and appropriate heat treatments resulted in a ferritic matrix microstructure with a 14% volume fraction of graphite nodules that are homogeneously distributed inside the matrix and are nearly spherical in shape with an average diameter of 45 μm. Young's modulus, yield stress and Poisson's ratio are equal to 175 GPa, 315 MPa, and 0.27, respectively. Carbon (nodules) and iron (matrix) have atomic numbers that are different enough to give a strong X-ray attenuation contrast so that the nodules, which act as natural markers for image correlation, are easily imaged by tomography.

To obtain a small fatigue pre-cracked specimen, a notched specimen with a $6 \times 4\,mm^2$ cross-section was machined from the heat treated cast iron bar and loaded in fatigue at a load ratio of 0.1. The specimen faces were mirror polished to enable for crack growth monitoring with a traveling optical microscope. A load-shedding technique was used to maintain the maximum SIF less than $12.8\,MPa\sqrt{m}$ in order to make sure that the plastic zone size (in plane strain) was less than 200 μm at the crack tip. Fatigue cycling was stopped as soon as the crack was about 1.5 mm in length. For the tomography experiment, two smaller dog-bone specimens with a $1.6 \times 1.6\,mm^2$ cross-section were spark cut inside the large sample so that each of them encompasses only a part of the crack front. As a result, one face of the small specimen studied herein contains the crack tip that was at the former surface of the larger sample (close to a plane stress condition) while the other face contains the crack tip that was at the center of the larger specimen (close to plane strain condition). Due to tunneling effect, the crack front in the studied sample is asymmetric, i.e. it is shorter on the former free surface and longer at the former center. For the sake of simplicity, the side corresponding to the former free surface (respectively former center) is referred to as short crack side (respectively long crack side) hereafter.

In situ Testing Procedure

The tomography experiment was performed on ID19 beamline at the European Synchrotron Radiation Facility (ESRF) in Grenoble, France. A monochromatic X-ray beam ($\Delta\lambda/\lambda = 10^{-2}$) having a photon energy of 60 keV traverses the sample (Fig. 1) giving a transmitted-to-incident intensity ratio of about 10%. To obtain a complete scan of the specimen cross-section in the vicinity of the crack, 600 radiographs were taken while the sample was rotating over 180° along its vertical axis; the total scan time was equal to 42 min. A Fast Readout Low Noise (FReLoN) 14-bit CCD camera with a 2048×2048 pixel chip was used. A specially designed fatigue machine[21] allows for in situ loading and high frequency cycling, i.e. up to 50 Hz, of the specimen. A PMMA tube, almost transparent to X-rays, is used as a load rig. The machine is directly mounted on the rotating stage of the beam line.

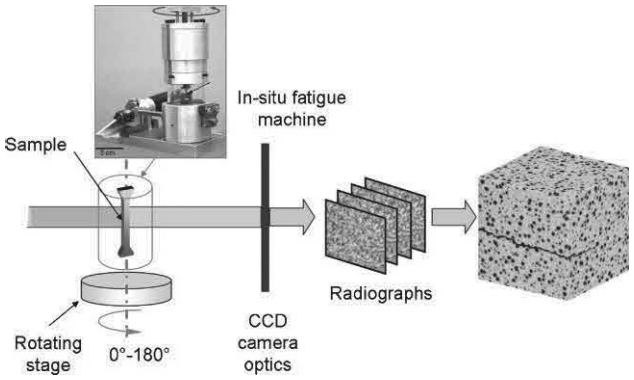

Fig. 1. Experimental setup used to perform in situ fatigue tests on beamline ID19 of ESRF. From the 600 radiographs, a reconstructed volume is obtained by using a filtered back-projection algorithm.

The tomography experiment was performed to obtain 3D pictures of the specimen during the initial loading cycle, and thereafter for different stages of cyclic loading. Therefore, the specimen was first gradually loaded up to a maximum level of 140 N, which is expected to result in a maximum SIF slightly less than the maximum value ($12.8\,MPa\sqrt{m}$) used in the fatigue pre-cracking test, and scans were acquired for intermediate loads of 50 and 100 N and for the maximum load step of 140 N. Then, the specimen was cycled at a load ratio of 0.1 under constant amplitude to propagate the crack and another scan was recorded after 30 000 fatigue cycles. Failure of the specimen occurred after 50 000 cycles.

Reconstruction of the tomographic data was performed with a conventional filtered back-projection algorithm.[22] It provides a 3D image with a grayscale colormap that is proportional to the local X-ray attenuation coefficient. The voxel size was chosen equal to 5.06 μm although better resolutions are achievable to visualize fatigue cracks with synchrotron microtomography.[7,11] This medium resolution is a good compromise between the quality of the image texture and the size of the reconstructed 3D images obtained from tomography. The chosen voxel size is much smaller than the relevant microstructure size, which is the size of the nodules, to allow for good quality images to be obtained while it is also large enough for the size of the region of interest (ROI), which was focused on the crack, to be only $340 \times 330 \times 512$ voxels. This limited data size enabled for the correlation computation

to be performed in real time during the tomography experiment (i.e., the computation time is less than the scan time on a PC with quad-core processor).

3D Displacement Measurement

3D displacements of any voxel of the 3D volume are assessed by using a volume correlation technique. The principle of volume correlation (or 3D-DVC) is to analyze two images of a solid under different loading conditions, and to determine the displacement field by searching for the best match between the images. Recently, a new formulation has been proposed that allows one to decompose the displacement field on an arbitrary chosen basis. One such basis can be finite element shape functions in two[20] or three dimensions.[15] The latter will be used herein. In the present case, 3D reconstructed volumes are considered, and 8-node elements defined on a 3D grid (tri-linear functions of x, y, and z [23]) may be chosen (it is designated as C8-DVC[15]).

A reference and loaded 3D images, $f(x,y,z)$ and $g(x,y,z)$, are assumed to be related through

$$g(x) = f(x + u(x))$$

where $\boldsymbol{u}$ is the searched displacement field. The latter is decomposed over a basis of functions

$$u(x) = \Sigma a_n N_n(x)$$

which is chosen in the sequel to be C8 finite element shape functions (eight node trilinear functions of x, y, and z over regular cubes)[23] and hence the method is designated as C8-DVC.[15] The unknown amplitudes are obtained through the minimization of

$$T(\{a\}) = ||g(x) - f(x + a_n N_n(x))||^2$$

A multiscale approach for this minimization is used to avoid secondary minima trapping, the details of which can be found in ref.[15]. Uncertainties in the displacement field determination can be estimated a priori, from a fake deformed image, g, which corresponds to a rigid translation of $^1/_2$ pixel in each space direction computed from f. Finally, once the minimization has been performed, the residual $g(x) - f(x + a_n N_n(x))$ shows the quality of the image registration.

SIF Extraction

From the measured displacement field, it is proposed to extract SIFs. First, least squares techniques are implemented by using 2D solutions.[24–27] An alternative technique to determine SIFs is to evaluate directly the J-integral along a given contour.[28] However, only few measurement data are used and strains and stresses are to be computed. To avoid this drawback, interaction integrals[29] are used for extracting SIFs from a discrete displacement field.[30,31] This last technique can be extended to the analysis of 3D cracks.[32] It will not be used in the following. Instead, the technique proposed by Hamam *et al*.[26] will be used.

It is assumed that each of the node layers orthogonal to the mean direction of the crack front can be treated separately. For each of these planes (nearly orthogonal to the crack front), the 3D displacement field is projected in a least squares sense onto a basis that includes 2D solutions for a cracked solid (mode I and mode II) as well as mode III asymptotic solutions. Following Williams,[33] a closed-form solution for the in-plane displacements $\underline{v}$ is derived from Kolossov–Muskhelishvili's potentials[34]

$$\underline{v}(r,\theta) = \sum_n [\omega_n \underline{\Omega}_n(r,\theta) + \upsilon_n \underline{\Upsilon}_n(r,\theta)] \tag{1}$$

where ω_n and υ_n are real numbers, n the number of terms of Williams' series, and so-called mode I

$$\begin{aligned}\underline{\Omega}_n = \frac{(-1)^{(1-n)/2}}{2\mu\sqrt{2\pi}} r^{n/2} \Big[\kappa \exp\Big(i\frac{n}{2}\theta\Big) - \frac{n}{2}\exp\Big\{i\Big(2-\frac{n}{2}\Big)\theta\Big\} \\ -\Big(1-\frac{n}{2}\Big)\exp\Big\{-i\frac{n}{2}\theta\Big\}\Big]\end{aligned} \tag{2}$$

and mode II

$$\begin{aligned}\underline{\Upsilon}_n = \frac{i(-1)^{(1-n)/2}}{2\mu\sqrt{2\pi}} r^{n/2} \Big[\kappa \exp\Big(i\frac{n}{2}\theta\Big) + \frac{n}{2}\exp\Big\{i\Big(2-\frac{n}{2}\Big)\theta\Big\} \\ -\Big(1+\frac{n}{2}\Big)\exp\Big\{-i\frac{n}{2}\theta\Big\}\Big]\end{aligned} \tag{3}$$

reference fields, r and θ denote the in-plane coordinates associated with the usual crack tip frame, μ Lamé's shear modulus, and κ dimensionless elastic (or Kolossov) coefficient related to Poisson's ratio ν according to $(3-\nu)/(1+\nu)$ for plane stress conditions or $3-4\nu$ for plane strain conditions (used in the sequel). The factor $\sqrt{2\pi}$ is introduced to match the usual definitions of the SIFs K_I and K_{II},[35] which are thus equal respectively to the amplitudes ω_1 and υ_1 associated with the fields Ω_1 and Υ_1.

Let us first note that the status of the fields Ω_n and Υ_n is very different for n less than or greater than 1. For $n > 1$, the fields are called here subsingular. They have no impact on the crack tip. Conversely, the attached stress fields increase with the distance to the crack tip. Such functions are thus useful to match the singular fields with the remote geometry, or boundary conditions. However, since their impact on the crack tip process zone is negligible, one does not insist here on the structure of these fields. For $n < 0$, the fields are referred to as supersingular. Traditionally, the supersingular fields are ignored because their asymptotic behavior near the crack tip is non-physical (i.e., diverging energy density). However, for the present purpose, since the crack tip process zone is cut out from the domain of analysis, one does not have to reject these solutions.[26]

Out of plane motions w induced by mode III displacements whose canonical field Ξ reads

$$\Xi = \frac{2}{\mu\sqrt{2\pi}} r^{1/2} \sin\left(\frac{\theta}{2}\right) \tag{4}$$

allow one to determine K_{III}.

Then, using least squares techniques, the measured displacement in each plane orthogonal to the crack front is

projected onto the considered basis function. In practice, in-plane solutions are considered for n ranging between –3 and 5. As mentioned above, negative n values correspond to supersingular solutions whose coefficients are related to a shift of the crack tip position in the plane with respect to the tip of the equivalent ''elastic crack'' for $n=-1$. By canceling out its contribution, the equivalent crack tip position is estimated.[26] A length scale proportional to the process zone size[26] is obtained when ω_{-3} is related to $\omega_1 = K_I$. As all odd n <0 functions lead to singular displacements at the crack tip, the displacement data at nodes whose distance to the crack tip (or respectively to the crack mouth) is less than 20, (resp. 10), voxels are not considered in the analysis.

Results

Uncertainty Analysis

A ROI of $288 \times 288 \times 288$ voxels centered on the assumed crack plane is considered (Figure 1). To evaluate measurement uncertainties, an a priori analysis is performed. Sub-voxel displacements are artificially applied to the reference picture and correlation computations are run for a sub-voxel increment of 0.1 when the prescribed displacement ranges between 0 and 1 voxels. In the present case, the mean error between the prescribed and measured displacements is an order of magnitude less than the corresponding standard deviation. Only the latter is discussed herein. Figure 2(a) shows the dependence of the standard displacement uncertainty with the prescribed displacement value. For any element size, the maximum uncertainty is obtained for $^1/_2$ voxel for which the interpolation biases are the highest. A symmetric response is observed with respect to that value, except for 8-voxel elements. For the latter, it is believed that the texture is too coarse in comparison with the element size to achieve good metrological result. Figure 2(b) shows the standard uncertainty as a function of the element size when the prescribed displacement is equal to 0.5 voxel. 16-voxel elements are chosen and lead to a measurement uncertainty of the order of 0.04 voxel. This value therefore corresponds to the resolution of the technique in the present case, and to a good compromise between measurement uncertainty and spatial resolution described by the power law interpolation (solid line) shown in Figure 2(b).

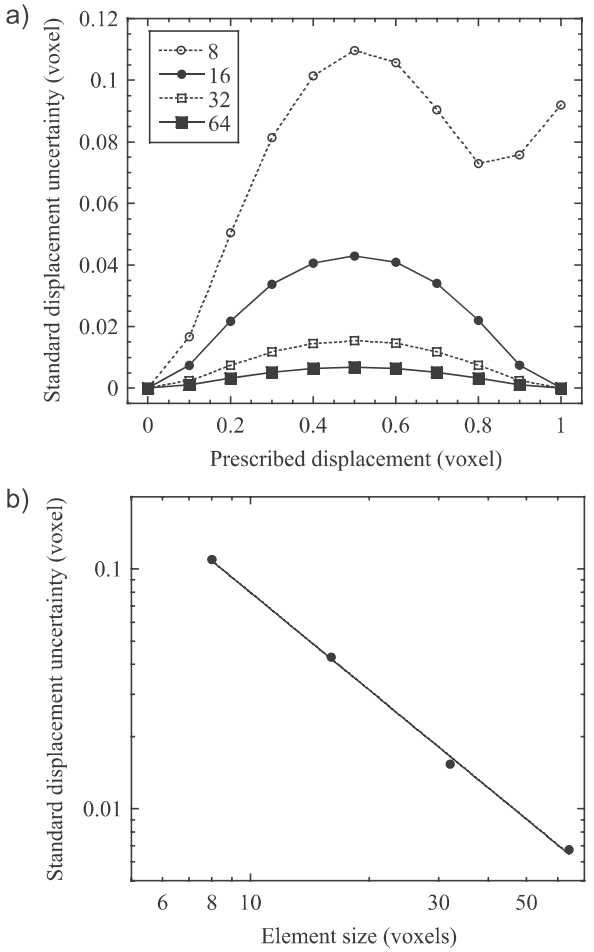

Fig. 2. Displacement uncertainty expressed in voxels as a function of the prescribed displacement for different element sizes (a). Maximum displacement uncertainty vs. element size (b). The solid line corresponds to a power law fit.

Figure 3 shows the displacement field obtained from DVC for the maximum load level of the first cycle. A clear discontinuity is observed for the displacement along the loading direction. In the other two directions, the discontinuities are less pronounced. The correlation residuals are low except in two regions [Fig. 3(b)]. First, around the rotation axis of the tomograph higher values are observed. This is due to reconstruction artifacts associated with the filtered back-projection algorithm.[22] Second, along the crack surface, the continuous kinematic basis is not adapted to fully capture discontinuous displacements induced by crack openings. This will allow the location of the crack surface to be deduced from

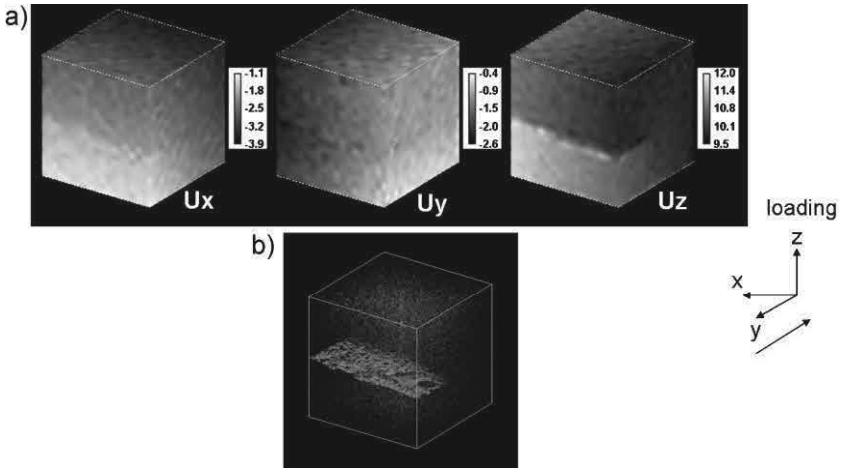

Fig. 3. (a) 3D displacement maps for maximum load level of the first cycle as obtained from the DVC analysis. The displacement levels are expressed in voxels (1 voxel ↔ 5.1 μm). (b) Thresholded correlation residuals showing reconstruction artifacts near the rotation axis and the crack surface.

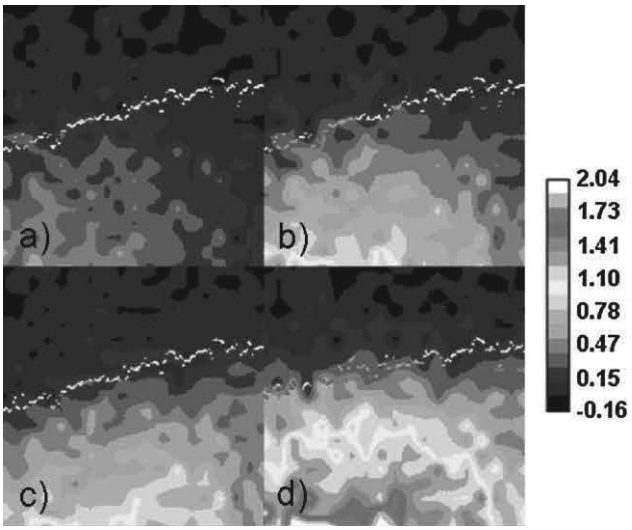

Fig. 4. COD maps (in voxels) at 50 N (a), 100 N (b), 140 N (c) for the first loading cycle, and at 130 N after 30 000 cycles (d). The crack tip positions (dotted white line) correspond to the maximum load levels of the two analyzed cycles.

the plane where the correlation residuals are maximum. From these raw results, two quantities are now extracted. First, CODs, and second, SIFs.

Crack Opening Displacement Analysis

The discontinuity due to the presence of a crack enables for the analysis of CODs. Away from the crack, the displacement field along the loading axis u_z [Fig. 3(a)] is smooth and continuous. Thus, the displacement jump on the crack surface, or COD, is estimated from the difference between two slices taken parallel to the crack plane on either side of the crack discontinuity in the u_z field. The resulting COD map is plotted in the specimen cross-section in Figure 4; the colormap used is proportional to the value of openings in voxels. Figure 4 shows that the crack opens more toward the short crack side while it remains closed at the tip toward the long crack side, i.e. the COD hardly reaches a 0.12 voxel value (or about 0.6 μm) even after 30 000 cycles and under maximum load [Fig. 4(d)]. From the a priori uncertainty analysis, it can be concluded that a 0.12-voxel COD is above the measurement uncertainty and can be considered as trustworthy. At 50 N, the crack is locally closed even toward the short crack side. It is only very close to the surface that Figure 4 shows COD values well above the uncertainty value. This tends to prove that opening occurs *locally* for a load value between 12 and 50 N. At 100 N, the crack is fully open on the short crack side of the specimen, i.e. from the surface to half the thickness of the sample, while the long crack side remains closed. The increase of the load up to 140 N further increases the COD values but the load is still not high enough to open the crack on the long crack side.

Crack Propagation Analysis

Information about the crack morphology is obtained both from the residual error map and from direct analysis of tomographic images. The residual error map shown in Figure 3(b) was proven superior to determine the 3D crack shape when the crack is open.[36] In nodular graphite cast iron, similarity of gray level between the crack surface and the graphite nodules makes the visualization of the crack front via image thresholding alone particularly difficult. However, when the crack tip does not open under load, the crack is not visible on the residual error map although residual opening inherited from pre-cracking makes the crack tip visible in the tomographic image. Thus, direct image analysis using ImageJ software[37] allows for the estimation of the crack tip position without any preliminary processing of the tomographic images.

The crack is observed on reconstructed images corresponding to y–z planes (Fig. 3) and an ImageJ plug-in enables one to retrieve the coordinates of the voxel that is manually selected as the crack tip for each slice through the sample thickness. This allows one to detect variations of the crack front position with increasing load or number of cycles (Fig. 5) provided the crack is sufficiently open. The crack lengths measured at the specimen surface with an optical microscope, at a better resolution than the tomographic images, are also plotted in Figure 5 for comparison purposes. On the short crack side, the crack length is apparently shorter at 12 N than at 50 N and above. This result should be considered with caution since the uncertainty in crack position is also greater at low load levels when the COD is small compared to the image resolution. However, the COD maps shown in Figure 4 also suggest that opening has occurred below 50 N on the short crack side, which tends to confirm that the apparent crack advance observed in Figure 5 is actually related to crack opening. After 30 000 cycles, the crack has visibly grown on the short crack side corresponding to higher values of COD [Fig. 4(b)] whereas it has apparently not grown on the long crack side where the COD maps show that the crack is still closed.

SIF Analysis

The evaluation of SIFs relies on the estimation of the position of the crack front in each analyzed plane. The in-plane

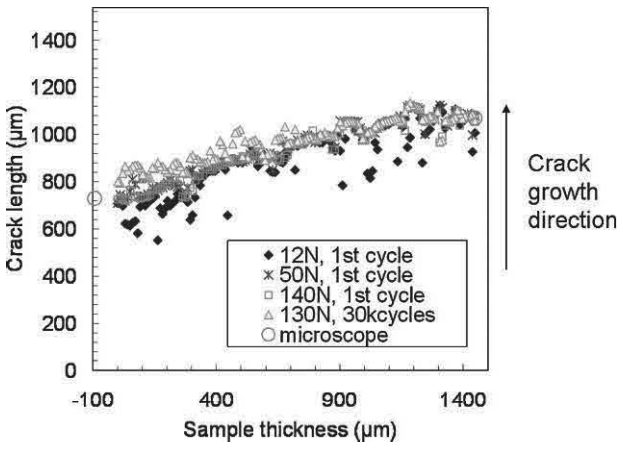

Fig. 5. Crack tip positions retrieved by manual tracking. Comparison with detections with an optical microscope (open circles shown on the sample sides).

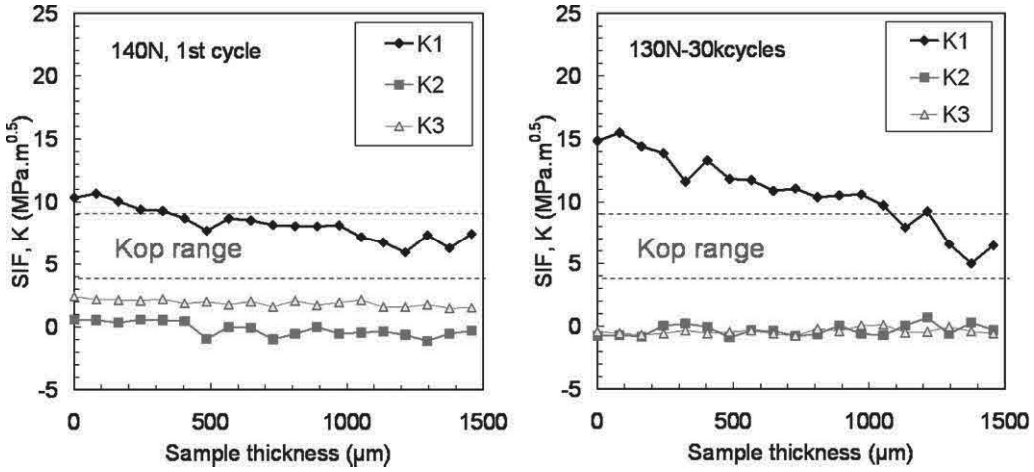

Fig. 6. SIF profiles for the two analyzed cycles.

displacement field is first interpolated by using a truncated expansion (1) with $-3 \leq n \leq 5$. The position such that the contribution of the first supersingular field ω_{-1} cancels out gives the sought location.[26] At this location, the SIFs are computed.

For the first cycle, the mode I SIF, K_I, is equal to about 10 MPa$\sqrt{}$m on the short crack side and 7 MPa$\sqrt{}$m on the other side (Fig. 6) for the maximum load level. After 30 000 fatigue cycles, K_I has remained almost the same on the long crack side whereas it has noticeably increased on the other side. The profile of K_{II} shows slight fluctuations around 0 through the sample thickness, which might be attributed to both image noise and computation uncertainty. K_{III} has a constant value of 2 MPa$\sqrt{}$m at the end of the first loading cycle, and it decreases to 0 after further cycling.

Discussion

To the best of the authors' knowledge, this is the first time that SIF values have been obtained within an opaque material using 3D-DVC. Compared with the discrete particle tracking measurements performed by Toda *et al.*[14], the DVC calculations presented herein have been used to produce COD maps and to correlate them with 3D tomographic observations of crack growth during in situ cycling. It appears very clearly (see Fig. 4 and 5) that crack growth occurs first in the zone of the crack front where the crack appears open on the COD maps (a value of 0.12 voxel for the u_z displacement is assumed to correspond to an opening of the crack). Those maps have been ''translated'' into K values, which allows for a more quantitative analysis of crack growth to be performed. Although K_{II} values are equal to zero along the crack front, positive values of K_{III} are obtained. They can possibly be ascribed to the crack shape and/or misalignment of the crack faces after fatigue pre-cracking of the large sample due to the change of testing conditions; very similar values for K_I, K_{II}, K_{III} have been obtained by Toda *et al.*[14] who used a similar experimental procedure to prepare and load their sample. After subsequent cycling however, mode II and III SIFs are vanishingly small and mode I is therefore predominant, as expected from the prescribed ''macroscopic'' mechanical testing conditions. However, it can be seen from Figure 6 that K_I increases when going from the long crack side toward the small crack side. Possible reasons for this evolution are discussed in the next paragraphs.

In the large sample that was pre-fatigued, the crack is longer in the center of the specimen than at the surface. This so-called tunneled crack shape[38,39] is the result of a balance between two conflicting effects. On the sample surface, the lack of constraint induces a larger crack tip plastic zone. The level of closure induced by this plastic zone (plasticity induced crack closure or PICC) is therefore higher close to the surface than at the center of the sample. For this reason, the effective SIF variation $\Delta K_{eff} = \Delta K_{max} - K_{op}$ (where K_{op} denotes the SIF at which the crack opens) is smaller close to the surface than in the bulk resulting in a slower growth of the crack close to the surface (tunneled shape). This effect can however be partially compensated by the fact that a locally lagging crack front induces a higher value of the SIF (*3D effect*).[40] During cycling, equilibrium is reached between the two effects and the crack propagates with a stable shape.[39]

In the small fatigue sample studied herein, however, the COD maps reveal that, for a given load level, crack opening is larger on the short crack side. This seems to indicate that the effect of the plastic zone size inherited from the large specimen has been cancelled out probably because the machining of the sample has induced some loss of constraint at the tip of the crack; the size of the remaining uncracked ligament is about 0.7 mm in the small sample while it was 3.6 mm in the large sample. Yet, because of the aforementioned 3D effect, higher SIF values are observed on the short crack side.

For the maximum load, K_I values obtained by DVC range from 10 MPa$\sqrt{}$m on the short crack side to 7 MPa$\sqrt{}$m on the long crack side, a value which is of the order of K_{op} for this material.[41–44] The crack driving force ΔK_{eff} is therefore small on the short crack side, and equal to zero on the long crack

side. This result is in agreement with those of Figure 5 that show a limited and asymmetric growth of the crack after 30 000 cycles. However, the small amount of growth obtained suffices to increase significantly the values of K_I above K_{op} to induce further growth and to lead to fracture after 20 000 additional cycles.

Conclusions

It was shown that X-ray computed micro-tomographic images acquired during in situ fatigue testing can be used to analyze the features of fatigue crack position and morphology and furthermore to *measure* SIFs all along the crack front, even for CODs as low as 1 μm.

This progress offers a comprehensive view of fatigue cracks in their full 3D expression, and reveals specifically 3D effects in fatigue crack propagation such as the influence of confined plasticity at the crack tip and the free edge effect where the crack front impinges. Further developments based on such an approach are expected to lead to effective crack propagation laws and their identification from experimental test with a full account of their complexity.

The same experiments have been performed with smaller increments of cycles to allow for tomographic scans to be acquired at numerous fractions of the total fatigue life. DVC calculations are used at different crack growth stages to study the variation of COD/SIF at the crack tip with propagation. Those experiments are currently being analyzed. Last, it is worth emphasizing that the same methodology can be applied on lab scale tomographs. Although additional imperfections of the imaging device are expected as compared to synchrotron light sources (e.g., lack of monochromaticity of the X-ray source, fictitious displacement due to temperature induced sample/source distance variations) which require a careful handling, a quantitative and trustworthy analysis of 3D cracks may still be performed.

[1] S. Suresh, *Fatigue of Materials*, Cambridge University Press, Cambridge **1991**.

[2] J. Baruchel, J.-Y. Buffière, E. Maire, P. Merle, G. Peix, *X-Ray Tomography in Material Sciences*, Hermes Science, Paris (France) **2000**.

[3] D. Bernard, Using synchrotron computed microtomography to quantify 3D micro geometrical changes in multimaterials, *Computational Methods and Experiments in Materials Characterisation II*, Wit Transactions on Engineering Sciences, Vol.: *51*, **2005**, pp. 217–227.

[4] J.-Y. Buffière, E. Maire, P. Cloetens, G. Lormand, R. Fougères, *Acta Mater.* **1999**, *47*, 1613.

[5] L. Babout, E. Maire, J.-Y. Buffière, R. Fougères, *Acta Mater.* **2001**, *49*, 2055.

[6] M. Preuss, P. J. Withers, E. Maire, J.-Y. Buffiere, *Acta Mater.* **2002**, *50*, 3177.

[7] W. Ludwig, J.-Y. Buffière, S. Savelli, P. Cloetens, *Acta Mater.* **2003**, *51*, 585.

[8] R. Sinclair, M. Preuss, E. Maire, J.-Y. Buffiere, P. Bowen, P. J. Withers, *Acta Mater.* **2004**, *52*, 1423.

[9] P. J. Schilling, B. R. Karedla, A. K. Tatiparthi, M. A. Verges, P. D. Herrington, *Comp. Sci. Technol.* **2005**, *65*, 2071.

[10] T. Rougelot, N. Burlion, D. Bernard, F. Skoczylas, Cracking due to leaching in cementitious composites: Experimental investigation by means of X-ray microtomography and numerical modeling, *Proceedings and Monographs in Engineering, Water and Earth Sciences*, Vol. *1–3*, **2007**, pp. 1797–1805.

[11] E. Ferrié, J.-Y. Buffiere, W. Ludwig, A. Gravouil, L. Edwards, *Acta Mater.* **2006**, *54*, 1111.

[12] A. Guvenilir, T. M. Breunig, J. H. Kinney, S. R. Stock, *Acta Mater.* **1997**, *45*, 1977.

[13] P. J. Withers, J. Bennett, Y.-C. Hung, M. Preuss, *Mater. Sci. Eng.* **2006**, *22*, 1052.

[14] H. Toda, I. Sinclair, J.-Y. Buffière, E. Maire, T. Connolley, M. Joyce, K. H. Khor, P. Gregson, *Philos. Mag.* **2003**, *83*, 2429.

[15] S. Roux, F. Hild, P. Viot, D. Bernard, *Comp. Part A* **2008**, *39*, 1253.

[16] M. A. Sutton, S. R. McNeill, J. D. Helm, Y. J. Chao, Advances in twodimensional and three dimensional computer vision, *Photomechanics, Topics in Applied Physics*, vol. *77*, Springer-Verlag, Berlin **2000**, pp. 323–372.

[17] B. K. Bay, T. S. Smith, D. P. Fyhrie, M. Saad, *Exp. Mech.* **1999**, *39*, 217.

[18] M. Bornert, J.-M. Chaix, P. Doumalin, J.-C. Dupré, T. Fournel, D. Jeulin, E. Maire, M. Moreaud, H. Moulinec, *Inst. Mes. Métrol.* **2004**, *4*, 43.

[19] E. Verhulp, B. van Rietbergen, R. Huiskes, *J. Biomech.* **2004**, *37*, 1313.

[20] G. Besnard, F. Hild, S. Roux, *Exp. Mech.* **2006**, *46*, 789.

[21] J.-Y. Buffière, E. Ferrié, H. Proudhon, W. Ludwig, *Mater. Sci. Technol.* **2006**, *22*, 1019.

[22] A. C. Kak, M. Slaney, Principles of Computerized Tomographic Imaging, *Society of Industrial and Applied Mathematics*, **2001**.

[23] O. C. Zienkievicz, R. L. Taylor, *The Finite Element Method*, McGraw-Hill, London, UK **1989**.

[24] S. R. McNeill, W. H. Peters, M. A. Sutton, *Eng. Fract. Mech.* **1987**, *28*, 101.

[25] J. Anbanto-Bueno, J. Lambros, *Eng. Fract. Mech.* **2002**, *69*, 1695.

[26] R. Hamam, F. Hild, S. Roux, *Strain* **2007**, *43*, 181.

[27] S. Yoneyama, T. Ogawa, Y. Kobayashi, *Eng. Fract. Mech.* **2007**, *74*, 1399.

[28] J. M. Huntley, J. E. Field, *Eng. Fract. Mech.* **1989**, *30*, 779.

[29] D. M. Parks, *Int. J. Fract.* **1974**, *10*, 487.

[30] J. Réthoré, A. Gravouil, F. Morestin, A. Combescure, *Int. J. Fract.* **2005**, *132*, 65.

[31] J. Réthoré, S. Roux, F. Hild, *Eng. Fract. Mech.* **2008**, *75*, 3763.
[32] M. Goz, J. Dolbow, B. Moran, *Int. J. Solids Struct.* **1998**, *35*, 1763.
[33] M. L. Williams, *ASME J. Appl. Mech.* **1957**, *24*, 109.
[34] N. I. Muskhelishvili, *Some Basic Problems of the Mathematical Theory of Elasticity*, P. Noordholl Ltd, Grönigen, Holland **1953**.
[35] G. R. Irwin, *ASME J. Appl. Mech.* **1957**, *24*, 361.
[36] J. Rannou, N. Limodin, J. Réthoré, A. Gravouil, W. Ludwig, M.-C. Baïetto-Dubourg, J.-Y. Buffière, A. Combescure, F. Hild, S. Roux, *Comp. Meth. Appl. Mech. Eng.* **2020**, *199*, 1307.
[37] ImageJ (**2008**), http://rsb.info.nih.gov/ij/.
[38] R. Branco, D. M. Rodrigues, F. V. Antunes, *Fat. Fract. Eng. Mater. Struct.* **2008**, *31*, 209.
[39] C.-Y. Hou, *Int. J. Fat.* **2008**, *30*, 1036.
[40] J. C. Newman, Jr, I. S. Raju, *Fracture Mechanics: 14th Symposium*, ASTM, Philadelphia, Pa (USA) **1983**, 238.
[41] P. Clément, J.-P. Angeli, A. Pineau, *Fat. Eng. Mater. Struct.* **1984**, *7*, 251.
[42] T. Ogawa, H. Kobayashi, *Fat. Fract. Eng. Mater. Struct.* **1987**, *10*, 273.
[43] M. Dahlber, *Int. J. Cast Met. Res.* **2004**, *17*, 29.
[44] J. Wasen, E. Heier, *Int. J. Fat.* **1998**, *20*, 737.